Macromolecular Rapid Communications

Macromolecular Rapid Communications
www.mrc-journal.de

RESEARCH ARTICLE

Amorphous Deposit Formed by Evaporation of Poly(Ethylene Glycol) Aqueous Droplet

Shengpei Shao[1] | Qingyou Liang[2] | Jiajia Zhou[3] | Xiangjun Gong[4] | Guangzhao Zhang[4]

[1]School of Marine Science and Engineering, South China University of Technology, Guangzhou, China | [2]Analytical and Testing Center, South China University of Technology, Guangzhou, China | [3]South China Advanced Institute for Soft Matter Science and Technology, School of Emergent Soft Matter, South China University of Technology, Guangzhou, China | [4]Faculty of Material Science and Engineering, South China University of Technology, Guangzhou, China

Correspondence: Jiajia Zhou (zhouj2@scut.edu.cn) | Xiangjun Gong (msxjgong@scut.edu.cn)

Received: 30 October 2025 | **Revised:** 18 December 2025 | **Accepted:** 20 December 2025

Keywords: deposit | drying | poly(ethylene glycol) (PEG) | polymer droplets

ABSTRACT

Crystallization of poly(ethylene glycol) (PEG) greatly debase the quality of printing and coating during drying, where it is used as a dispersant. In this work, we have investigated the drying process of aqueous droplet of poly(ethylene glycol) (PEG) as a function of molecular weight (M_w). It shows that PEG would crystallize on a hydrophilic surface but form an amorphous deposit on a hydrophobic surface at a humidity (RH) of 40% when M_w ≤5000 g/mol. However, PEG would crystallize regardless of the surface and RH when M_w is above 10 000 and 20 000 g/mol. By regulating PEG concentration, molecular weight, and RH, the droplet can be dried into an amorphous deposit for over 24 h. Raman spectroscopy and low-field nuclear magnetic resonance (LF-NMR) indicate that the water molecules bound to PEG chains (M_w ≤5000 g/mol) under slow drying inhibit their crystallization.

1 | Introduction

The evaporation of droplets on solid surfaces is a fundamental issue that underpins numerous industrial applications, including inkjet printing [1], spray coating [2], pharmaceutical processing [3], and functional surface fabrication [4]. The morphology of the final deposit critically determines the performance, including mechanical properties [5], biocompatibility [6], and optical properties [7] of these applications. The drying behavior of surface droplets has been extensively characterized. The "coffee-ring" effect, first described by Deegan et al., occurs when outward capillary flow transports solutes toward the pinned contact line, creating ring-like deposits [8, 9]. This phenomenon is governed by differential evaporation rates across the droplet surface, with enhanced evaporation at the edge driving internal flow patterns [10]. External conditions significantly influence this process: substrate wettability controls contact line dynamics and evaporation geometry [11], while ambient temperature and RH affect evaporation kinetics and solute transport [12, 13].

The introduction of polymers alters droplet drying dynamics. High molecular weight polymers increase solution viscosity, modify internal flow patterns, and suppress the coffee-ring effect through viscoelastic mechanisms [14, 15]. Due to the biocompatibility, non-toxicity, and exceptional protein-resistance properties, PEG has found applications in biomedical devices, coatings [16–18], where it was used as a dispersant to regulate viscosity and colloidal stability [19, 20] or to control the deposition in dispersion systems like ink [21] and coatings [22]. The controlled deposition of PEG from evaporating droplets is therefore of considerable technological importance. Polymer-solvent interactions, particularly for PEG with its strong hydrogen bonding to water, create concentration gradients that influence both flow behavior and phase transition kinetics [23, 24]. Therefore, the evaporation kinetics of polymer solutions is profoundly influenced by the molecular weight of the polymer. High molecular weight polymer usually reduces the evaporation rate since it increases viscosity and decreases the molecular mobility [25, 26]. Recent theoretical work demonstrates that polymer solution exhibits diffusion-

limited evaporation dynamics, where the buildup of a high-concentration polymer layer at the solution-air interface creates an evaporation rate that scales with time [27]. Environmental conditions significantly affect this process. The wettability of a droplet on a substrate determines its contact line dynamics and geometry [28], while RH and temperature control evaporation rate and the time available for molecular reorganization [29].

For crystallizable PEG, the final deposit morphology depends on the competition between crystallization and becoming glassy during drying. When polymer concentration is above the saturated concentration during evaporation, the polymer would either undergo crystallization to form ordered structures or is kinetically trapped in an amorphous or glassy state [30]. The crystallization of polymer depends on its molecular mobility, nucleation barriers, and the available time for chain organization [26]. Molecular simulation reveals that an amorphous state emerges when the dehydration rate exceeds that of polymer chains organizing into ordered crystalline structures [31]. Environmental RH also plays an important role. High RH can slow down the rate of water removal, favorable for the amorphous formation by maintaining molecular mobility while preventing effective nucleation [29]. Note that amorphous and crystalline polymers exhibit quite different mechanical, optical, and dissolution properties. However, although polymer crystallization kinetics has been extensively studied, the formation and stabilization of amorphous polymer deposits remain largely unclear.

In this work, we have investigated the evaporation of an aqueous PEG droplet. The factors determining the crystalline or amorphous state of the deposits were examined. We demonstrate that the droplet can be dried into an amorphous deposit for a long time by regulating the concentration and molecular weight of PEG as well as RH. This study provides an approach to prepare crystalline or amorphous polymer deposits by liquid droplet drying.

2 | Materials and Methods

2.1 | Materials

PEG samples with molecular weights of 1000 g/mol (PEG-1K), 5000 g/mol (PEG-5K), 10 000 g/mol (PEG-10K), and 20 000 g/mol (PEG-20K) were purchased from Shanghai Macklin Biochemical Co. and used as received without further purification. 11-mercapto-1-undecanol ($HS(CH_2)_{11}OH$, 97%) and 1-dodecanethiol ($CH_3(CH_2)_{11}SH$, 98%) were from the same supplier. Deionized (DI) water with a resistivity of 18.2 MΩ cm was used to prepare all aqueous solutions. PEG solutions were prepared at concentrations ranging from 20 to 500 mg/mL (corresponding to 2–50 wt.%) to investigate concentration effects on drying behavior.

2.2 | Surface Preparation

Glass slide (76.2 × 25.4 × 1.2 mm, SAGA, China) was cleaned using piranha solution (98% H_2SO_4: 30% H_2O_2, 7:3 v/v) at 90°C for 2 h followed by sonication in ethanol and deionized water for 10 min to remove organic contaminants. After drying under nitrogen, the slide was sputter-coated with a 3-nm titanium adhesion layer followed by a 3-nm gold layer using a Denton Desk V sputter system (Figure S1a,b). Self-assembled monolayer (SAMs) [32] was prepared by immersing the gold-coated substrate in 1.0 mM solution of either 1-dodecanethiol (for hydrophobic surface) or 11-mercapto-1-undecanol (for hydrophilic surface) in ethanol for 24 h at room temperature, the resulting surface had water contact angle of 95° ± 2° (hydrophobic, —CH_3 terminated) and 46° ± 2° (hydrophilic, —OH terminated), respectively (Figure S1c–e).

2.3 | Observation of the Droplet Drying Process

Droplet drying experiments were conducted in a controlled-environment chamber with programmable temperature and RH control (Figure 1a). PEG solution droplets (0.5 μL) were deposited on the prepared glass surfaces using a micropipette. After droplet deposition, drying was monitored by optical microscopy at 25°C under RH of 20%, 40%, and 60%. Monitoring continued for up to 10 min or until the droplet volume no longer changed.

The side (TD-4KHU, 2.0 μm/pixel, SANQTID, China) and bottom-mounted (UC30S, 2.0 μm/pixel, MOKOSE, China) cameras simultaneously capture time-lapse images at a rate of 1 frames/s to map the morphological evolution of the deposits. The side camera captures variations in the droplet contact angle, while the bottom camera records changes in the radius of the basal circle, thereby allowing the calculation of droplet volume variations using Equation (1):

$$V = \frac{\pi}{3} \times \left[\left(\frac{r}{\sin\theta} \times (1 - cos\theta) \right)^2 \times \left(\frac{3r}{\sin\theta} - \frac{r}{\sin\theta}(1 - cos\theta) \right) \right] \tag{1}$$

where θ is the contact angle, and r is the radius of the basal circle.

2.4 | Polarized Light Microscope

The state of the PEG droplets after drying (30 min after deposition) was observed through a polarized light microscope (Axio Scope A1, Zeiss), capturing time-lapse images with an exposure duration of 125 ms. Evaporation-induced crystallization in PEG droplets manifests a two-level optical birefringence phenomenon, which is absent in the non-crystalline state. The percentage of crystalline area within the total deposited area was defined as the ratio of the area exhibiting birefringence through polarized imaging to the total deposition area of the droplet through bright field imaging.

2.5 | In Situ X-Ray Scattering Measurements

X-ray diffraction (XRD) studies of the sediments were conducted on an X'pert Powder X-ray diffractometer using CuKα radiation (λ = 1.5418 Å) with a diffraction angle range of 10 to 90 degrees.

2.6 | Raman Spectroscopy

Molecular structure analysis was performed using a LabRAM Aramis Raman spectrometer (HORIBA Jobin-Yvon) with a

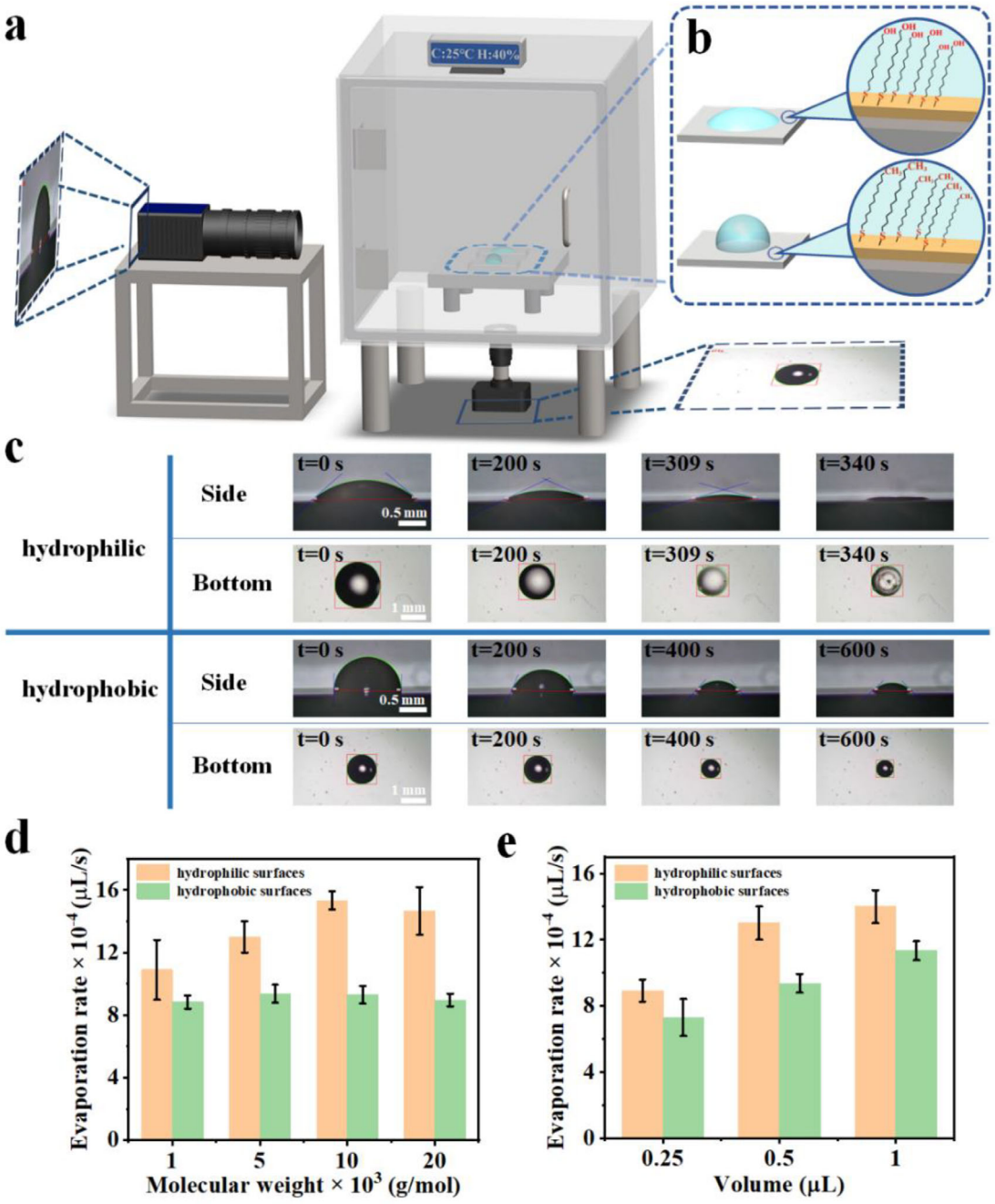

FIGURE 1 | Experimental setup for real-time imaging of PEG droplet drying dynamics. (a) Schematic diagram of the controlled-environment chamber equipped with dual-view imaging systems (side-view and bottom-view) for droplet evaporation studies. (b) Substrate configurations: hydrophilic glass (—OH terminated) and hydrophobic glass ($—CH_3$ terminated). (c) Representative side-view and bottom-view images of a PEG-5K droplet on hydrophilic and hydrophobic substrates during the drying process. (d) Averaged evaporation rate during drying of 0.5 μL PEG droplets with different molecular weights on both substrate types. (e) Averaged evaporation rate during drying of PEG-5K droplets with varying volumes on both substrate types. For panels (c–d), conditions are held constant at 25°C and 40% RH, with a PEG concentration of 60 mg/mL for all molecular weights.

785 nm laser and 10× objective lens (numerical aperture 0.10). Spectra were recorded in the range of 2600–3600 cm^{-1} with two accumulations and 30 s per scan to monitor changes in polymer conformation and water coordination during the drying process.

2.7 | Low-Field NMR (LF-NMR)

Water dynamics in PEG solutions were characterized using a Bruker mq20 bench-top NMR spectrometer operating at 20 MHz. The Carr–Purcell–Meiboom–Gill (CPMG) pulse sequence was employed to measure spin-spin relaxation times (T_2). Measurements were performed at 25°C with 1600 data points per scan, eight scans averaged, and a repetition delay of 15 s. The CONTIN algorithm was used for T_2 distribution analysis to distinguish between free and bound water components using the equation below:

$$M(t) = \sum_j I_j e^{\left(-\frac{t}{T_{2j}}\right)} \quad (2)$$

where I_j is the signal intensity of component j, and its corresponding spin-spin relaxation time is represented as T_{2j}. The distribution of T_{2j} is characterized by the optimal relaxation time. The peak area is defined as the sum of all intensity values across the distribution. Apparent evaporation time was further defined as the time required for the droplet to go from its initial PEG concentration to that used in LF-NMR under specific conditions:

$$\text{Apparent evaporation time} = \frac{V}{\text{Evaporation rate}} \tag{3}$$

where V is the volume evaporated to the corresponding concentration, the evaporation rate was measured by our experiments shown in Figure 1.

3 | Results and Discussion

3.1 | Characterization of the Droplet Drying Process

A dual-view imaging system (side-view and bottom-view) was used to monitor droplet evaporation, with precisely controlled ambient RH and temperature to regulate evaporation rates (Figure 1a). Substrate wettability determines contact line dynamics during drying (Figure 1b). On hydrophobic surfaces, reduced wetting produced distinct evaporation profiles compared to hydrophilic substrates [33]. Dual-view imaging tracked contact angle and base area changes throughout drying, suggesting that PEG droplets tend to crystallize on the surface of hydrophilic substrates and form an amorphous state on hydrophobic surfaces (Figure 1c). Real-time side-view images suggest the droplet contact angles decreased with increasing PEG concentration on both substrates using this imaging apparatus (Figure S2 and Videos S1 and S2). In particular, droplets (volume: 0.5 μL) of PEG solutions (initial concentration: 60 mg/mL) with varying molecular weight were imaged on both substrate types and dried at 25°C, 40% relative RH. On hydrophilic substrates, PEG droplets initially showed pinned contact lines (~40° contact angle, 800–900 μm radius) for 130–150 s, followed by depinning with two-phase evolution: constant contact angle (80 s), then linear decrease (70 s) with concurrent radius reduction to ~600 μm (Figure S2a–c and Video S1). In particular, PEG-20K droplets crystallized immediately after contact angles reached 12° without depinning. On hydrophobic substrates, evaporation was more complex (Figure S2d–f and Video S2). Initial pinning lasted 150–180 s with linear contact angle decrease at constant radius (~85° contact angle, 500–600 μm radius). When contact angles reached critical values, contact lines retracted through rapid jumping motions, establishing new pinning positions [33]. This cycle repeated multiple times, producing stepwise radius reduction and sawtooth-like contact angle variations. The longer pinning duration on hydrophobic surfaces results from slower droplet shape changes [34, 35]. Meanwhile, PEG-5K droplets of different volumes showed similar evaporation behaviors: single pinning on hydrophilic surfaces vs. multiple pinning phases on hydrophobic surfaces (Figure S3).

Based on the above observations, droplets spread more on hydrophilic surfaces compared to hydrophobic surfaces, increasing contact area and accelerating water removal. Meanwhile, the evaporation rates decrease with increasing PEG molecular weight and concentration on both substrates (Figure 1d), while the evaporation rates increase with droplet volume (Figure 1e). As shown in Figure S2c, the volume of the droplets of PEG-5K, PEG-10K, and PEG-20K slightly changed after 309, 269, and 180 s, respectively, and the droplet began to crystallize on the hydrophilic substrates. In contrast, the volume of the droplet of PEG-1K remained unchanged after 330 s but formed an amorphous deposit. A distinct difference in crystallization behavior was observed on hydrophobic substrates: PEG-10K and PEG-20K began to crystallize at a later time, i.e., 433 and 354 s, respectively; whereas PEG-1K and PEG-5K stabilized in volume after 450 s and remained amorphous. (Figure S2f). These molecular weight-dependent behaviors result from increased solution viscosity that creates diffusion barriers, hindering water transport to the evaporation interface [14]. The volume effect reflects the direct relationship between surface area and evaporation flux, where larger droplets provide greater evaporation area [34]. High polymer concentrations further enhance this viscosity-controlled transport mechanism, particularly pronounced for longer polymers [36].

3.2 | Deposition Patterns of PEG Droplets After Drying

Deposition patterns of dried droplets were analyzed using bottom-view bright-field and polarization imaging after the side-view images showed no further volumetric changes for over 30 min. Different molecular weights under different RH conditions yielded distinct final states: PEG-1K and PEG-5K remained amorphous, while PEG-10K and PEG-20K crystallized. Especially, PEG-1K did not crystallize under all tested conditions (Figure S4), whereas PEG-10K and PEG-20K crystallized consistently (Figures S5 and S6). Among all the samples, PEG-5K showed intermediate behavior with variable outcomes (Figure 2). This molecular weight dependence on crystallization ability aligns with the reported critical molecular weight thresholds for PEG crystallization [35].

In Figure 2, both RH and initial PEG concentration modulated final deposit states through evaporation kinetics for PEG-5K. At low RH (RH = 20%), rapid water loss promoted crystal formation by concentrating polymer chains quickly, the proportion of crystallization area reached 100% for all the samples with varying initial concentration on hydrophilic surfaces, whereas on hydrophobic surfaces, despite the occurrence of crystallization, it remained generally limited. As concentration increases from 2% to 10%, the percentage of crystalline area increased from 45% to 83%. In addition, for RH = 40%, PEG-5K with an initial concentration of 6 wt.% crystallized on a hydrophilic surface, but formed an amorphous deposit on a hydrophobic surface. Even at a higher concentration of 10 wt.%, the percentage of crystalline area was consistently lower on hydrophobic surfaces than on hydrophilic surfaces. For higher RH (RH = 60%), an amorphous deposit also formed on hydrophilic surfaces for concentrations of 2 and 6 wt.%, which may be attributed to the reason that slowed evaporation extends the time for chain reorganization and hinders crystallization (blue regions in Figure 2). A lower initial concentration of 2 wt.%) increased intermolecular spacing, which suppressed

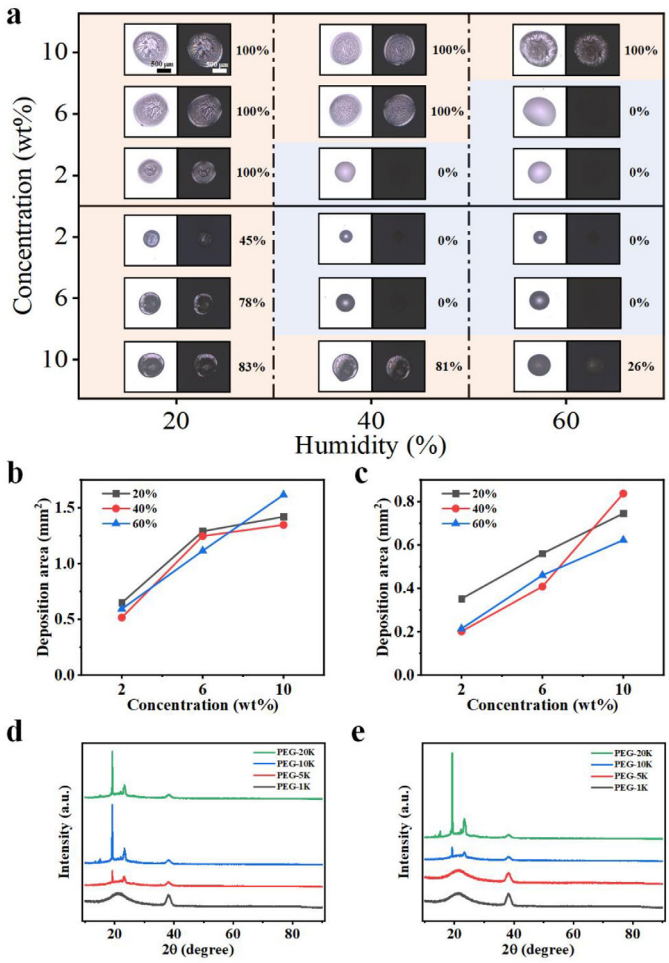

FIGURE 2 | Phase diagram of PEG-5K droplet crystallization as a functions of concentration and RH. (a) Crystalline (orange) and non-crystalline (blue) regions for PEG-5K droplets on hydrophilic (upper panel) and hydrophobic (lower panel) substrates. The right-hand value shows the percentage of crystalline area within the total deposited area. Bright-field micrographs (white background) and polarized light images (black background) show representative deposit morphologies. Deposition area corresponding to concentration on hydrophilic (b) and hydrophobic (c) surfaces. XRD patterns of the deposition regions of PEG droplets (25°C, 40% RH, 6 wt.%) on hydrophilic (d) and hydrophobic (e) surfaces.

nucleation efficiency, resulted in an amorphous deposit on both hydrophilic and hydrophobic surfaces. At a high concentration (10 wt.%), nucleation efficacy was enhanced by the increased molecular density, it crystallized at all RH. With the RH increased from 20% to 60%. the percentage of crystalline area decreased from 83% to 26% on the hydrophobic surface. Meanwhile, the deposition area expanded with increasing concentration on both hydrophilic and hydrophobic surfaces, which accelerated the evaporation rate and promoted crystal formation (Figure 2b,c; Figures S4b,c–S6b,c). Consequently, increasing concentration promotes crystallization, whereas high RH facilitates amorphous deposit. To obtain detailed structural information, XRD were applied to analyze the deposition patterns formed from 6 wt.% PEG droplets dried under 40% RH conditions. The amorphous deposits exhibit broad and diffuse diffraction peaks characteristic of disordered structures. In contrast, the crystalline deposits display two distinct Bragg diffraction peaks at approximately 19.2° and 23.3° (2θ). The sharp peak profiles and well-resolved baseline separation confirm the formation of long-range ordered, highly oriented crystalline structures (Figure 2d,e). The crystallization behavior observed here reflects the competition between solvent removal rate and polymer chain ordering kinetics [37]. Slower evaporation on hydrophobic surfaces provides extended time for chain mobility, but insufficient concentration gradients can prevent effective nucleation, resulting in amorphous state formation under specific RH-concentration combinations [38]. Similarly, small-volume PEG-5K droplets (0.25, 0.5 μL) on hydrophobic surfaces exhibited amorphous deposit behavior, while larger droplets (1 μL) crystallized (Figure S3g). This volume-dependent crystallization still correlates with evaporation rate differences, namely large-volume droplets demonstrate a higher evaporation rate, which accelerates the nucleation of PEG molecular chains and promotes more rapid crystal formation.

3.3 | Molecular Dynamics During Droplet Drying Revealed by Raman Spectroscopy and Low-Field NMR

To investigate molecular-level changes of PEG and water during drying, PEG-5K droplets (0.5 μL, 6 wt.%) were deposited on substrates with different wettability and analyzed by Raman spectroscopy at 25°C and 40% RH in Figure 3. As shown in Figure 3a,b,

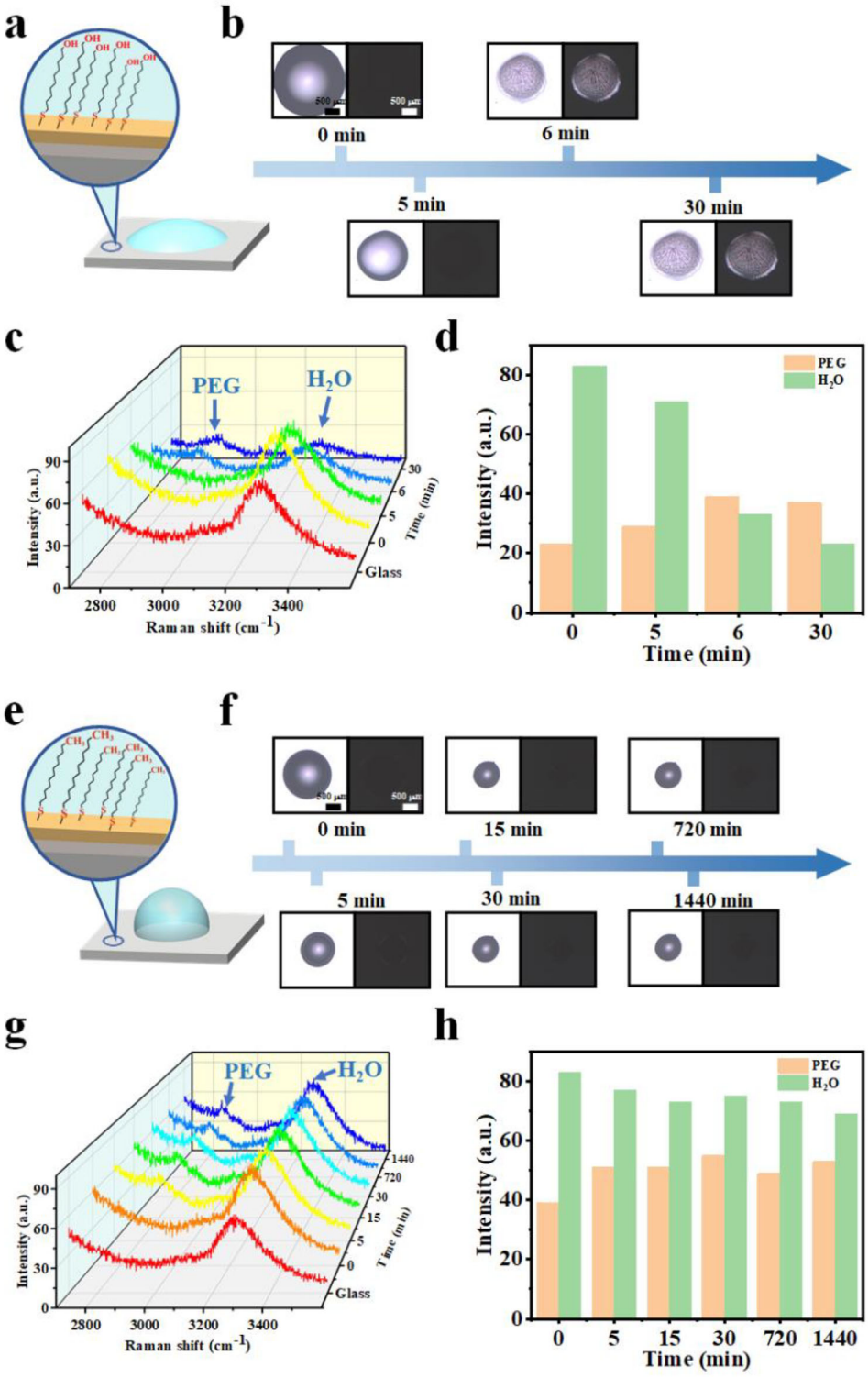

FIGURE 3 | Real-time Raman spectroscopy analysis of PEG-5K droplet drying dynamics (25°C, 40% RH, 6 wt.%). Time-lapse morphology and corresponding Raman spectra (2600–3600 cm^{-1}) during droplet evaporation on (a–d) hydrophilic (—OH) and (e–h) hydrophobic ($—CH_2$) surfaces. Spectra track molecular conformational changes. Scale bar: 500 μm.

bright-field micrographs (white background) and polarized light images (black background) were recorded at multiple representative stages during droplet evaporation on hydrophilic surfaces. The spectra revealed two characteristic peaks: $—CH_2$ stretching vibrations at 2892 cm^{-1} from PEG segments and —OH stretching vibrations at 3292 cm^{-1} from water molecules [39] (Figure 3c,g). In Figure 3d, for PEG-5K, no $—CH_2$ peak appeared initially (5 min), while the —OH peak remained strong, while PEG-1K showed no detectable $—CH_2$ peaks throughout drying, consistent with its non-crystalline state (Figure S7a–d). The absence of the —OH peak suggested that the amount of PEG molecules in the illumination area of Raman spectroscopy were not enough to

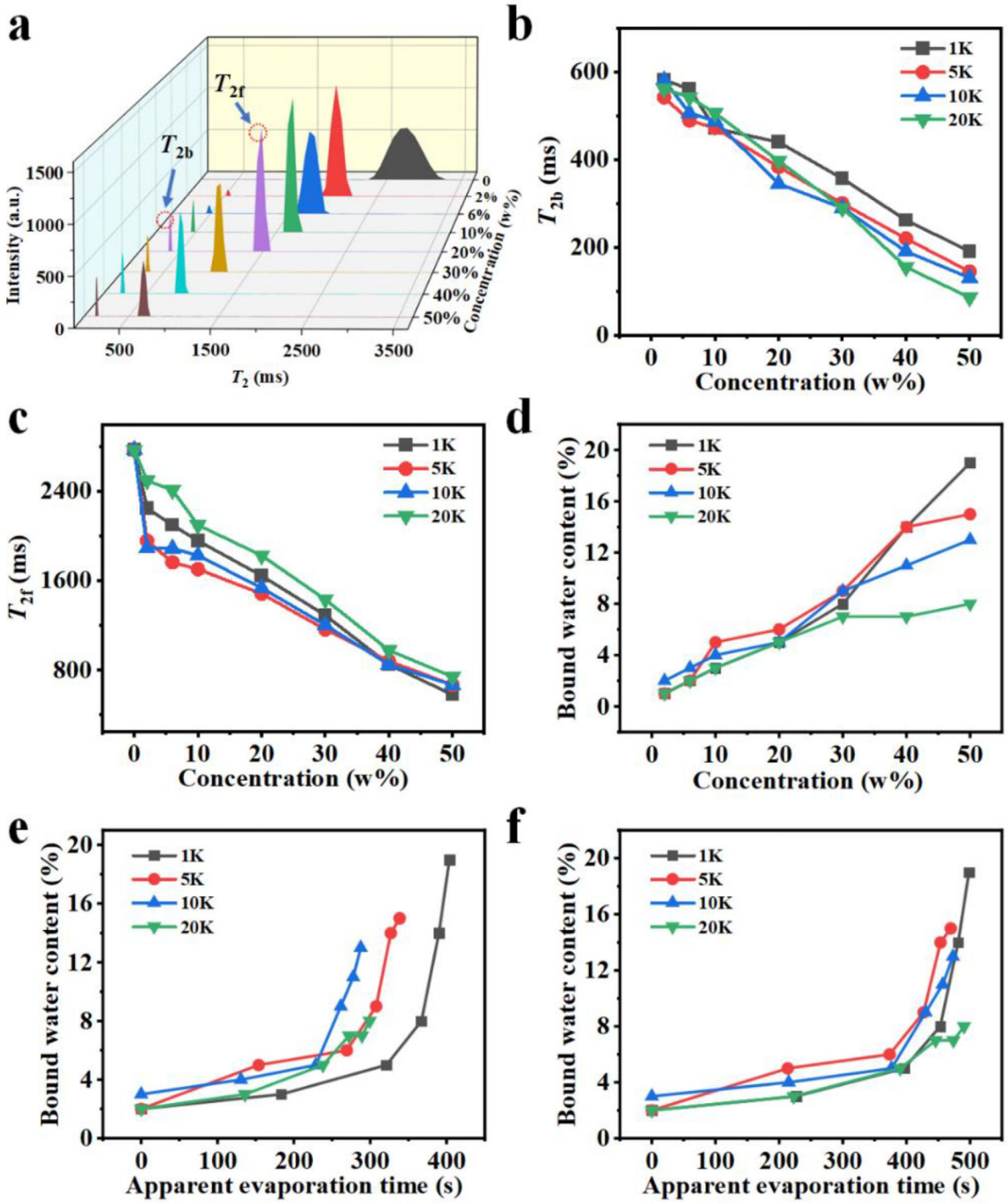

FIGURE 4 | Water dynamics in PEG solutions characterized by low-field NMR. (a) Distribution of spin-spin relaxation times (T_2) for PEG-5K/water mixtures at varying concentration. Distinct peaks indicate free and bound water, while T_{2f} and T_{2b} denote their respective relaxation time. T_{2f} profiles for (b) free water and T_{2b} profiles for (c). (d) Bound water components in PEG solutions in dependence of concentrations for varying PEG molecular weights. Bound water components in PEG solutions in dependence of apparent evaporation time on hydrophilic (e) and hydrophobic (f) surfaces for varying PEG molecular weights. It was noted that apparent evaporation time was defined as the time required for the droplet on a specific surface to go from its initial PEG concentration to that used in LF-NMR under specific conditions based on the evaporation rate measured in Figure 1.

be detected. From Figure 3c,d, the —CH_2 peak emerged and increases gradually with the progress of crystallization (~6 min), coinciding with a significant reduction in the —OH peak due to water loss on hydrophilic surfaces. PEG-10K showed similar behaviors to that of PEG-5K (Figure S8a–d). PEG-20K exhibited similar crystallization timing but weaker —CH_2 signals, likely due to thin crystalline layers below Raman detection limits (Figure S9a–d).

On hydrophobic substrates, bright-field micrographs (white background) and polarized light images (black background) recorded several typical moments during the evaporation of a droplet, spherical droplet geometry slowed evaporation and altered deposition patterns (Figure 3e,f). Notably, —CH_2 peaks appeared earlier across all molecular weights, even in non-crystalline states. PEG-1K developed detectable —CH_2 peaks after 5 min despite remaining amorphous (Figure S7e–h). Similarly, PEG-

5K showed —CH_2 peaks at 5 min without crystallizing, with both spectroscopic signatures persisting after 24 h (Figure 3g,h). In contrast with Figure 3d,h showed the —OH peak slightly decreased, while the —CH_2 peak slightly increased for droplets on hydrophobic surfaces, with the relatively slow evaporation rate of water, and PEG did not rapidly become more concentrated either, so this peak did not change much. For crystalline PEG-10K and PEG-20K, the —CH_2 signal increased while the —OH signal decreased (Figures S8e–h and S9e–h). It should be noted that at the late stage of drying, the —CH_2 peak appeared earlier and was stronger on hydrophobic surfaces than on hydrophilic surfaces, because hydrophilic droplets spread into thinner films, leaving less PEG within the illumination spot of the Raman spectroscopy, which may remain undetectable.

To further probe water dynamics during droplet drying, we used low-field NMR to measure the relaxation time of water molecules as the concentration increased in the droplet. From the above results, both PEG-1k and PEG-5k droplets can end up amorphous deposit, a state where most free water has evaporated while hydrogen-bonded bound water forms a shell around each PEG chain [24].

The drying process can be modeled as a continuous increase of PEG concentration within the binary system. NMR relaxation time measurements (T_2) effectively captured the dynamic behavior of both components as functions of concentration (Figure 4a). T_2 relaxation distinguished two distinct proton populations: exchangeable protons from free water molecules (T_{2f} ~2771 ms) and non-exchangeable protons from bound water (T_{2b} ~542 ms) influenced by hydrogen bonding [40, 41]. It should be noted that the T_{2b} signal was attributed to the bound water instead of protons on EG. This is because T_2 from protons on EG was commonly smaller than 200 ms [24] and comparably weak in contrast of the protons on bound water due to a much lower ratio of EG. In PEG solutions with concentration ranging from 10 to 50 wt.%, the molar ratio of EG units varies between 22 to 2.4. As the PEG chain becomes longer, both T_{2f} and T_{2b} decreases, indicating that the hydration layer becomes more tightly bound (Figure 4b,c). Tighter binding promotes PEG chain rearrangement, whereas looser binding hinders rapid reorganization of chains [24]. Previous results were reported that M_W does not change how many waters can bind per EG unit, but it does change the binding structure of those water molecules near the chain [24].

In addition, the corresponding peak area was defined as the sum of the intensities at all collected data points within in the peak, representing the total content of free water and bound water, respectively (Figure S10a–f). As the droplet dries and PEG concentration rises, free water decreases and bound water increases. Meanwhile, as the molecular weight of PEG increases, the overall content of bound water decreases (Figure 4d; Figure S10). Before drying, bound water forms a hydration layer that keeps PEG chains apart and limits their motion. Similar to the trends of T_{2f} and T_{2b}, the free water evaporates and the ratio of bound water rises correspondingly as PEG concentration increases (Figure 4d). A higher amount ratio of bound water appears for shorter polymer chains, preventing them from coming close for crystallization.

Furthermore, "apparent evaporation time" was defined as the time required for the droplet to go from its initial PEG concentration to that used in LF-NMR under specific conditions (i.e., faster evaporation on hydrophilic surfaces or slower evaporation on hydrophobic surfaces). It is deduced as the ratio of the evaporation amount of water in droplets to the evaporation rate of PEG droplets with different molecular weights on hydrophilic (Figure 4e) and hydrophobic (Figure 4f) surfaces based on Figure 1d (see Methods). As shown in both Figure 4e,f, as the molecular weight of PEG increases, the overall content of bound water decreases. Meanwhile, bound water remains upon hydrophobic surfaces (Figure 4f) with a slower evaporation rate so that chains cannot get close, giving an amorphous deposit. In contrast, bound water amount decreases with fast drying (i.e., upon hydrophilic surfaces in Figure 4e), chains come closer, and crystallization is more likely. These results provide molecular evidence supporting the observed drying behaviors: the bound water was strongly affected by the molecular weight of PEG, as short chains promote a high degree of hydration with more bound water; Meanwhile, hydrophilic surfaces promote rapid water evaporation and reduce bound water formation thus favoring crystallization, while hydrophobic surfaces retain bound water particularly for short chains, making them more likely to form amorphous state.

4 | Conclusion

This study demonstrates systematic control over crystalline vs. amorphous deposit formation in drying PEG droplets through manipulation of molecular weight, RH, concentration, and substrate wettability. In particular, the molecular weight of PEG plays a critical role in the final deposit state by binding different amount of water near it. PEG-1K consistently forms amorphous deposits, while PEG-10K and PEG-20K readily crystallize under all tested conditions. PEG-5K exhibits tunable behavior: hydrophilic surfaces promote crystallization through rapid water removal, while hydrophobic surfaces at elevated RH favor amorphous formation by retaining bound water that disrupts polymer chain ordering. These findings provide a framework for engineering polymer deposits with controlled phase distributions in printing, coating, and biomedical applications.

Author Contributions

X.G. and G.Z. designed the study. S.S. carried out analysis, characterization, and processing of experimental data. Q.L. conducted Raman spectroscopy detection. X.G., J.Z., G.Z., and S.S. wrote the manuscript. All authors discussed the results and commented on the manuscript.

Acknowledgements

This work was financially supported by the Key-Area Research and Development Program of Guangdong Province (2023B0101200006), the Guangdong Basic and Applied Basic Research Foundation (grant number 2024A1515011926), the Fund of Guangdong Provincial Key Laboratory of Luminescence from Molecular Aggregates, Guangzhou 510640, China (South China University of Technology) (grant number 2023B1212060003), and State Key Laboratory of Applied Microbiology Southern China (grant number SKLAM008-2022).

Conflicts of Interest

The authors declare no conflicts of interest.

Data Availability Statement

The data that support the findings of this study are available in the supplementary material of this article.

References

1. B. Derby, "Inkjet Printing of Functional and Structural Materials: Fluid Property Requirements, Feature Stability, and Resolution," *Annual Review of Materials Research* 40 (2010): 395–414, https://doi.org/10.1146/annurev-matsci-070909-104502.

2. A. F. Routh, "Drying of Thin Colloidal Films," *Reports on Progress in Physics* 76 (2013): 046603, https://doi.org/10.1088/0034-4885/76/4/046603.

3. S. V. Bhujbal, B. Mitra, U. Jain, et al., "Pharmaceutical Amorphous Solid Dispersion: A Review of Manufacturing Strategies," *Acta Pharmaceutica Sinica B* 11 (2021): 2505–2536, https://doi.org/10.1016/j.apsb.2021.05.014.

4. S. Zhu, Y. Tang, C. Lin, X. Y. Liu, and Y. Lin, "Recent Advances in Patterning Natural Polymers: From Nanofabrication Techniques to Applications," *Small Methods* 5 (2021): 2001060, https://doi.org/10.1002/smtd.202001060.

5. J. J. Cooper-White, R. C. Crooks, K. Chockalingam, and D. V. Boger, "Dynamics of Polymer−Surfactant Complexes: Elongational Properties and Drop Impact Behavior," *Industrial & Engineering Chemistry Research* 41 (2002): 6443–6459.

6. M. Mastiani, N. Firoozi, N. Petrozzi, S. Seo, and M. Kim, "Polymer-Salt Aqueous Two-Phase System (ATPS) Micro-Droplets for Cell Encapsulation," *Scientific Reports* 9 (2019): 15561, https://doi.org/10.1038/s41598-019-51958-4.

7. T. Song and W. Shi, "Polymer Crystallization and Optical Birefringence Modulated by Solvent Evaporation in Sessile Droplets," *Polymer* 307 (2024): 127287, https://doi.org/10.1016/j.polymer.2024.127287.

8. R. D. Deegan, O. Bakajin, T. F. Dupont, G. Huber, S. R. Nagel, and T. A. Witten, "Capillary Flow as the Cause of Ring Stains from Dried Liquid Drops," *Nature* 389 (1997): 827–829, https://doi.org/10.1038/39827.

9. R. D. Deegan, "Pattern Formation in Drying Drops," *Physical Review E* 61 (2000): 475–485, https://doi.org/10.1103/PhysRevE.61.475.

10. R. G. Larson, "Transport and Deposition Patterns in Drying Sessile Droplets," *AIChE Journal* 60 (2014): 1538–1571, https://doi.org/10.1002/aic.14338.

11. R. G. Picknett and R. Bexon, "The Evaporation of Sessile or Pendant Drops in Still Air," *Journal of Colloid and Interface Science* 61 (1977): 336–350, https://doi.org/10.1016/0021-9797(77)90396-4.

12. J. M. Stauber, S. K. Wilson, B. R. Duffy, and K. Sefiane, "On the Lifetimes of Evaporating Droplets," *Journal of Fluid Mechanics* 744 (2014): R2, https://doi.org/10.1017/jfm.2014.94.

13. K. Sefiane and R. Bennacer, "Nanofluids Droplets Evaporation Kinetics and Wetting Dynamics on Rough Heated Substrates," *Advances in Colloid and Interface Science* 147–148 (2009): 263–271, https://doi.org/10.1016/j.cis.2008.09.011.

14. K. A. Baldwin and D. J. Fairhurst, "The Effects of Molecular Weight, Evaporation Rate and Polymer Concentration on Pillar Formation in Drying Poly(Ethylene Oxide) Droplets," *Colloids and Surfaces A: Physicochemical and Engineering Aspects* 441 (2014): 867–871, https://doi.org/10.1016/j.colsurfa.2012.10.049.

15. G. K. S. Raghuram, L. Bansal, S. Basu, and A. Kumar, "Suppression of Coffee Ring Effect in High Molecular Weight Polyacrylamide Droplets Evaporating on Hydrophobic Surfaces," *Colloids and Surfaces A: Physicochemical and Engineering Aspects* 612 (2021): 126002, https://doi.org/10.1016/j.colsurfa.2020.126002.

16. C. A. Finch, "Poly(Ethylene Glycol) Chemistry: Biotechnical and Biomedical Applications. Edited by J. Milton Harris. Plenum Publishing, New York, 1992. ISBN 0-306-44078-4," *Polymer International* 33 (1994): 115, https://doi.org/10.1002/pi.1994.210330114.

17. K. Knop, R. Hoogenboom, D. Fischer, and U. S. Schubert, "Poly(Ethylene Glycol) in Drug Delivery: Pros and Cons As Well as Potential Alternatives," *Angewandte Chemie International Edition* 49 (2010): 6288–6308.

18. S. Chen, L. Li, C. Zhao, and J. Zheng, "Surface Hydration: Principles and Applications Toward Low-Fouling/Nonfouling Biomaterials," *Polymer* 51 (2010): 5283–5293, https://doi.org/10.1016/j.polymer.2010.08.022.

19. M. Prawatborisut, F. Seidi, D. Yiamsawas, and D. Crespy, "PEGylation of Shellac-Based Nanocarriers for Enhanced Colloidal Stability," *Colloids and Surfaces B: Biointerfaces* 183 (2019): 110434, https://doi.org/10.1016/j.colsurfb.2019.110434.

20. J. O. Han, H. J. Lee, and B. Jeong, "Thermosensitive Core-Rigid Micelles of Monomethoxy Poly(Ethylene Glycol)-Deoxy Cholic Acid," *Biomaterials Research* 26: 16, https://doi.org/10.1186/s40824-022-00263-9.

21. S. K. Tam, K. Y. Fung, G. S. H. Poon, and K. M. Ng, "Product Design: Metal Nanoparticle-Based Conductive Inkjet Inks," *AIChE Journal* 62 (2016): 2740–2753, https://doi.org/10.1002/aic.15271.

22. H. Lee, S.-T. Tsai, P.-H. Wu, W.-P. Dow, and C.-M. Chen, "Influence of Additives on Electroplated Copper Films and Their Solder Joints," *Materials Characterization* 147 (2019): 57–63, https://doi.org/10.1016/j.matchar.2018.10.029.

23. M. Z. Jora, M. V. C. Cardoso, and E. Sabadini, "Dynamical Aspects of Water-Poly(Ethylene Glycol) Solutions Studied by ^{1}H NMR," *Journal of Molecular Liquids* 222 (2016): 94–100, https://doi.org/10.1016/j.molliq.2016.06.101.

24. J. Wu and S. Chen, "Investigation of the Hydration of Nonfouling Material Poly(Ethylene Glycol) by Low-Field Nuclear Magnetic Resonance," *Langmuir* 28 (2012): 2137–2144, https://doi.org/10.1021/la203827h.

25. D. Mamalis, V. Koutsos, K. Sefiane, A. Kagkoura, M. Kalloudis, and M. E. R. Shanahan, "Effect of Poly(Ethylene Oxide) Molecular Weight on the Pinning and Pillar Formation of Evaporating Sessile Droplets: The Role of the Interface," *Langmuir* 31 (2015): 5908–5918, https://doi.org/10.1021/la504905y.

26. J. A. Baird, B. Van Eerdenbrugh, and L. S. A. Taylor, "A Classification System to Assess the Crystallization Tendency of Organic Molecules from Undercooled Melts," *Journal of Pharmaceutical Sciences* 99 (2010): 3787–3806, https://doi.org/10.1002/jps.22197.

27. M. Huisman, W. C. K. Poon, P. B. Warren, S. Titmuss, and D. Marenduzzo, "Diffusive Evaporation Dynamics in Polymer Solutions is Ubiquitous," *Soft Matter* 21 (2025): 1508–1515, https://doi.org/10.1039/D4SM01215A.

28. P. G. Pittoni, C.-C. Chang, T.-S. Yu, and S.-Y. Lin, "Evaporation of Water Drops on Polymer Surfaces: Pinning, Depinning and Dynamics of the Triple Line," *Colloids and Surfaces A: Physicochemical and Engineering Aspects* 432 (2013): 89–98, https://doi.org/10.1016/j.colsurfa.2013.04.045.

29. J. A. Baird, R. Olayo-Valles, C. Rinaldi, and L. S. Taylor, "Effect of Molecular Weight, Temperature, and Additives on the Moisture Sorption Properties of Polyethylene Glycol," *Journal of Pharmaceutical Sciences* 99 (2010): 154–168, https://doi.org/10.1002/jps.21808.

30. P. Mahawar, M. Praveena, S. Bhuyan, D. S. Pillai, and S. Chandran, "Pattern Formation in Evaporating Polymer Solutions—Interplay Between Dewetting and Decomposition," *ACS Polymers Au* 4 (2024): 302–310.

31. A. Paajanen, A. Rinta-Paavola, and J. Vaari, "High-Temperature Decomposition of Amorphous and Crystalline Cellulose: Reactive Molecular Simulations," *Cellulose* 28 (2021): 8987–9005.

32. X. Huang, C. Li, K. Zuo, and Q. Li, "Predominant Effect of Material Surface Hydrophobicity on Gypsum Scale Formation," *Environmental*

Science & Technology 54 (2020): 15395–15404, https://doi.org/10.1021/acs.est.0c03826.

33. Q. Li, P. Zhou, and H. J. Yan, "Pinning–Depinning Mechanism of the Contact Line During Evaporation on Chemically Patterned Surfaces: A Lattice Boltzmann Study," *Langmuir* 32 (2016): 9389–9396, https://doi.org/10.1021/acs.langmuir.6b01490.

34. M. M. U. Rehman, A. Askounis, and G. Nagayama, "Effect of Surface Wettability on Evaporation Rate of Droplet Array," *Physics of Fluids* 35 (2023): 037121, https://doi.org/10.1063/5.0137614.

35. C. Qiao, S. Jiang, D. Dong, X. Ji, L. An, and B. Jiang, "The Critical Lowest Molecular Weight for PEG to Crystallize in Cross-Linked Networks," *Macromolecular Rapid Communications* 25 (2004): 659–663, https://doi.org/10.1002/marc.200300113.

36. E. Caicedo-Casso, J. Sargent, R. M. Dorin, et al., "A Rheometry Method to Assess the Evaporation-Induced Mechanical Strength Development of Polymer Solutions Used for Membrane Applications," *Journal of Applied Polymer Science* 136 (2019): 47038, https://doi.org/10.1002/app.47038.

37. S. Karimi, I. Ghasemi, F. Abbassi-Sourki, M. Samara, and N. R. Demarquette, "PEG-Grafted Graphene/PLLA Nanocomposites: Effect of PEG Chain Length on Crystallization Kinetics of PLLA," *ACS Omega* 7 (2022): 31197–31204, https://doi.org/10.1021/acsomega.2c03397.

38. S. Andjelić and R. C. Scogna, "Polymer Crystallization Rate Challenges: The Art of Chemistry and Processing," *Journal of Applied Polymer Science* 132 (2015): 42066.

39. V. V. Kuzmin, V. S. Novikov, L. Y. Ustynyuk, K. A. Prokhorov, E. A. Sagitova, and G. Y. Nikolaeva, "Raman Spectra of Polyethylene Glycols: Comparative Experimental and DFT Study," *Journal of Molecular Structure* 1217 (2020): 128331, https://doi.org/10.1016/j.molstruc.2020.128331.

40. J. Chen, X. Gong, C. Zeng, Y. Wang, and G. Zhang, "Mechanical Insight into Resistance of Betaine to Urea-Induced Protein Denaturation," *The Journal of Physical Chemistry B* 120 (2016): 12327–12333, https://doi.org/10.1021/acs.jpcb.6b10172.

41. S. Lüsse and K. Arnold, "The Interaction of Poly(Ethylene Glycol) With Water Studied by ^{1}H and ^{2}H NMR Relaxation Time Measurements," *Macromolecules* 29 (1996): 4251–4257.

Supporting Information

Additional supporting information can be found online in the Supporting Information section.

Supporting File 1: marc70187-sup-0001-SuppMat.docx.

Supporting File 2: marc70187-sup-0002-VideoS1.mp4.

Supporting File 3: marc70187-sup-0003-VideoS2.mp4.